



HAL
open science

X-Ray Polarization of BL Lacertae in Outburst

Abel L. Peirson, Michela Negro, Ioannis Liodakis, Riccardo Middei, Dawoon E. Kim, Alan P. Marscher, Herman L. Marshall, Luigi Pacciani, Roger W. Romani, Kinwah Wu, et al.

► **To cite this version:**

Abel L. Peirson, Michela Negro, Ioannis Liodakis, Riccardo Middei, Dawoon E. Kim, et al.. X-Ray Polarization of BL Lacertae in Outburst. *The Astrophysical journal letters*, 2023, 948, 10.3847/2041-8213/acd242 . insu-04102297

HAL Id: insu-04102297

<https://insu.hal.science/insu-04102297>

Submitted on 22 May 2023

HAL is a multi-disciplinary open access archive for the deposit and dissemination of scientific research documents, whether they are published or not. The documents may come from teaching and research institutions in France or abroad, or from public or private research centers.

L'archive ouverte pluridisciplinaire **HAL**, est destinée au dépôt et à la diffusion de documents scientifiques de niveau recherche, publiés ou non, émanant des établissements d'enseignement et de recherche français ou étrangers, des laboratoires publics ou privés.



Distributed under a Creative Commons Attribution 4.0 International License



X-Ray Polarization of BL Lacertae in Outburst

Abel L. Peirson¹, Michela Negro^{2,3,4}, Ioannis Liodakis⁵, Riccardo Middei^{6,7}, Dawoon E. Kim^{8,9,10}, Alan P. Marscher¹¹, Herman L. Marshall¹², Luigi Pacciani⁸, Roger W. Romani¹, Kinwah Wu¹³, Alessandro Di Marco⁸, Niccolò Di Lalla¹, Nicola Omodei¹, Svetlana G. Jorstad^{11,14}, Iván Agudo¹⁵, Pouya M. Kouch^{5,16}, Elina Lindfors⁵, Francisco José Aceituno¹⁵, Maria I. Bernardos¹⁵, Giacomo Bonnoli^{15,17}, Víctor Casanova¹⁵, Maya García-Comas¹⁵, Beatriz Agís-González¹⁵, César Husillos¹⁵, Alessandro Marchini¹⁸, Alfredo Sota¹⁵, Carolina Casadio^{19,20}, Juan Escudero¹⁵, Ioannis Myserlis^{21,22}, Albrecht Sievers²¹, Mark Gurwell²³, Ramprasad Rao²³, Ryo Imazawa²⁴, Mahito Sasada²⁵, Yasushi Fukazawa^{24,26,27}, Koji S. Kawabata^{24,26,27}, Makoto Uemura^{24,26,27}, Tsunefumi Mizuno²⁸, Tatsuya Nakaoka²⁶, Hiroshi Akitaya²⁹, Yeon Cheong^{30,31}, Hyeon-Woo Jeong^{30,31}, Sincheol Kang³⁰, Sang-Hyun Kim^{30,31}, Sang-Sung Lee^{30,31}, Emmanouil Angelakis³², Alexander Kraus²², Nicolò Cibrario³³, Immacolata Donnarumma³⁴, Juri Poutanen¹⁷, Fabrizio Tavecchio¹⁷, Lucio A. Antonelli^{6,7}, Matteo Bachetti³⁵, Luca Baldini^{36,37}, Wayne H. Baumgartner³⁸, Ronaldo Bellazzini³⁶, Stefano Bianchi³⁹, Stephen D. Bongiorno³⁸, Raffaella Bonino^{40,41}, Alessandro Brez³⁶, Niccolò Bucciantini^{42,43,44}, Fiamma Capitanio⁸, Simone Castellano³⁶, Elisabetta Cavazzuti³⁴, Chien-Ting Chen⁴⁵, Stefano Ciprini^{6,46}, Enrico Costa⁸, Alessandra De Rosa⁸, Ettore Del Monte⁸, Laura Di Gesu³⁴, Victor Doroshenko⁴⁷, Michal Dovčiak⁴⁸, Steven R. Ehlert³⁸, Teruaki Enoto⁴⁹, Yuri Evangelista⁸, Sergio Fabiani⁸, Riccardo Ferrazzoli⁸, Javier A. Garcia⁵⁰, Shuichi Gunji⁵¹, Kiyoshi Hayashida⁵², Jeremy Heyl⁵³, Wataru Iwakiri⁵⁴, Philip Kaaret³⁸, Vladimir Karas⁴⁸, Takao Kitaguchi⁴⁹, Jeffery J. Kolodziejczak³⁸, Henric Krawczynski⁵⁵, Fabio La Monaca⁸, Luca Latronico⁴⁰, Grzegorz Madejski¹, Simone Maldera⁴⁰, Alberto Manfreda³⁶, Frédéric Marin⁵⁶, Andrea Marinucci³⁴, Francesco Massaro^{40,41}, Giorgio Matt³⁹, Ikuyuki Mitsuishi⁵⁷, Fabio Muleri⁸, C.-Y. Ng⁵⁸, Stephen L. O'Dell³⁸, Chiara Oppedisano⁴⁰, Alessandro Papitto⁷, George G. Pavlov⁵⁹, Matteo Perri^{6,7}, Melissa Pesce-Rollins³⁶, Pierre-Olivier Petrucci⁶⁰, Maura Pilia³⁵, Andrea Possenti³⁵, Simonetta Puccetti⁶, Brian D. Ramsey³⁸, John Rankin⁸, Ajay Ratheesh⁸, Oliver J. Roberts⁴⁵, Carmelo Sgró³⁶, Patrick Slane⁶¹, Paolo Soffitta⁸, Gloria Spandre³⁶, Douglas A. Swartz⁴⁵, Toru Tamagawa⁴⁹, Roberto Taverna⁶², Yuzuru Tawara⁵⁷, Allyn F. Tennant³⁸, Nicholas E. Thomas³⁸, Francesco Tombesi^{46,63,64}, Alessio Trois³⁵, Sergey Tsygankov¹⁷, Roberto Turolla^{13,62}, Jacco Vink⁶⁵, Martin C. Weisskopf³⁸, Fei Xie^{8,66}, and Silvia Zane¹³

¹ Department of Physics and Kavli Institute for Particle Astrophysics and Cosmology, Stanford University, Stanford, CA 94305, USA; alpy95@stanford.edu

² University of Maryland, Baltimore County, Baltimore, MD 21250, USA

³ NASA Goddard Space Flight Center, Greenbelt, MD 20771, USA

⁴ Center for Research and Exploration in Space Science and Technology, NASA/GSFC, Greenbelt, MD 20771, USA

⁵ Finnish Centre for Astronomy with ESO, University of Turku, FI-20014 Turku, Finland

⁶ Space Science Data Center, Agenzia Spaziale Italiana, Via del Politecnico snc, I-00133 Roma, Italy

⁷ INAF Osservatorio Astronomico di Roma, Via Frascati 33, I-00078 Monte Porzio Catone (RM), Italy

⁸ INAF Istituto di Astrofisica e Planetologia Spaziali, Via del Fosso del Cavaliere 100, I-00133 Roma, Italy

⁹ Dipartimento di Fisica, Università degli Studi di Roma “La Sapienza”, Piazzale Aldo Moro 5, I-00185 Roma, Italy

¹⁰ Dipartimento di Fisica, Università degli Studi di Roma “Tor Vergata”, Via della Ricerca Scientifica 1, I-00133 Roma, Italy

¹¹ Institute for Astrophysical Research, Boston University, 725 Commonwealth Avenue, Boston, MA 02215, USA

¹² MIT Kavli Institute for Astrophysics and Space Research, Massachusetts Institute of Technology, 77 Massachusetts Avenue, Cambridge, MA 02139, USA

¹⁴ Mullard Space Science Laboratory, University College London, Holmbury St. Mary, Dorking, Surrey RH5 6NT, UK

¹⁵ Astronomical Institute, St. Petersburg State University, 28 Universitetsky prospekt, Peterhof, St. Petersburg 198504, Russia

¹⁶ Instituto de Astrofísica de Andalucía, IAA-CSIC, Glorieta de la Astronomía s/n, E-18008 Granada, Spain

¹⁷ Department of Physics and Astronomy, University of Turku, FI-20014 Turku, Finland

¹⁸ INAF Osservatorio Astronomico di Brera, Via E. Bianchi 46, I-23807 Merate (LC), Italy

¹⁹ University of Siena, Astronomical Observatory, Via Roma 56, I-53100 Siena, Italy

²⁰ Institute of Astrophysics, Foundation for Research and Technology - Hellas, Voutes, 7110 Heraklion, Greece

²¹ Department of Physics, University of Crete, 70013 Heraklion, Greece

²² Institut de Radioastronomie Millimétrique, Avenida Divina Pastora, 7, Local 20, E-18012 Granada, Spain

²³ Max-Planck-Institut für Radioastronomie, Auf dem Hügel 69, D-53121 Bonn, Germany

²⁴ Center for Astrophysics—Harvard & Smithsonian, 60 Garden Street, Cambridge, MA 02138 USA

²⁵ Department of Physics, Graduate School of Advanced Science and Engineering, Hiroshima University Kagamiyama, 1-3-1 Higashi-Hiroshima, Hiroshima 739-8526, Japan

²⁶ Department of Physics, Tokyo Institute of Technology, 2-12-1 Ookayama, Meguro-ku, Tokyo 152-8551, Japan

²⁷ Hiroshima Astrophysical Science Center, Hiroshima University 1-3-1 Kagamiyama, Higashi-Hiroshima, Hiroshima 739-8526, Japan

²⁸ Core Research for Energetic Universe (Core-U), Hiroshima University, 1-3-1 Kagamiyama, Higashi-Hiroshima, Hiroshima 739-8526, Japan

²⁹ Hiroshima Astrophysical Science Center, Hiroshima University, 1-3-1 Kagamiyama, Higashi-Hiroshima, Hiroshima 739-8526, Japan

³⁰ Planetary Exploration Research Center, Chiba Institute of Technology 2-17-1 Tsudanuma, Narashino, Chiba 275-0016, Japan

³¹ Korea Astronomy & Space Science Institute, Daedeokdae-ro 776, Yuseong-gu, Daejeon 34055, Republic Of Korea

³² University of Science and Technology, Gajeong-ro 217, Yuseong-gu, Daejeon 34113, Republic Of Korea

³³ Section of Astrophysics, Astronomy & Mechanics, Department of Physics, National and Kapodistrian University of Athens, Panepistimiopolis Zografos 15784, Greece

³⁴ Dipartimento di Fisica, Università degli Studi di Torino, Via Pietro Giuria 1, I-10125 Torino, Italy

³⁵ ASI - Agenzia Spaziale Italiana, Via del Politecnico snc, I-00133 Roma, Italy

³⁷ INAF Osservatorio Astronomico di Cagliari, Via della Scienza 5, I-09047 Selargius (CA), Italy

³⁸ Istituto Nazionale di Fisica Nucleare, Sezione di Pisa, Largo B. Pontecorvo 3, I-56127 Pisa, Italy

- ³⁹ Dipartimento di Fisica, Università di Pisa, Largo B. Pontecorvo 3, I-56127 Pisa, Italy
- ⁴⁰ NASA Marshall Space Flight Center, Huntsville, AL 35812, USA
- ⁴¹ Dipartimento di Matematica e Fisica, Università degli Studi Roma Tre, Via della Vasca Navale 84, I-00146 Roma, Italy
- ⁴² Istituto Nazionale di Fisica Nucleare, Sezione di Torino, Via Pietro Giuria 1, I-10125 Torino, Italy
- ⁴³ Dipartimento di Fisica, Università degli Studi di Torino, Via Pietro Giuria 1, I-10125 Torino, Italy
- ⁴⁴ INAF Osservatorio Astrofisico di Arcetri, Largo Enrico Fermi 5, I-50125 Firenze, Italy
- ⁴⁵ Dipartimento di Fisica e Astronomia, Università degli Studi di Firenze, Via Sansone 1, I-50019 Sesto Fiorentino (FI), Italy
- ⁴⁶ Istituto Nazionale di Fisica Nucleare, Sezione di Firenze, Via Sansone 1, I-50019 Sesto Fiorentino (FI), Italy
- ⁴⁷ Science and Technology Institute, Universities Space Research Association, Huntsville, AL 35805, USA
- ⁴⁸ Istituto Nazionale di Fisica Nucleare, Sezione di Roma “Tor Vergata”, Via della Ricerca Scientifica 1, I-00133 Roma, Italy
- ⁴⁹ Institut für Astronomie und Astrophysik, Universität Tübingen, Sand 1, D-72076 Tübingen, Germany
- ⁵⁰ Astronomical Institute of the Czech Academy of Sciences, Boční II 1401/1, 14100 Praha 4, Prague, Czech Republic
- ⁵¹ RIKEN Cluster for Pioneering Research, 2-1 Hirosawa, Wako, Saitama 351-0198, Japan
- ⁵² California Institute of Technology, Pasadena, CA 91125, USA
- ⁵³ Yamagata University, 1-4-12 Kojirakawa-machi, Yamagata-shi 990-8560, Japan
- ⁵⁴ Osaka University, 1-1 Yamadaoka, Suita, Osaka 565-0871, Japan
- ⁵⁵ University of British Columbia, Vancouver, BC V6T 1Z4, Canada
- ⁵⁶ International Center for Hadron Astrophysics, Chiba University, Chiba 263-8522, Japan
- ⁵⁷ Physics Department and McDonnell Center for the Space Sciences, Washington University in St. Louis, St. Louis, MO 63130, USA
- ⁵⁸ Université de Strasbourg, CNRS, Observatoire Astronomique de Strasbourg, UMR 7550, F-67000 Strasbourg, France
- ⁵⁹ Graduate School of Science, Division of Particle and Astrophysical Science, Nagoya University, Furo-cho, Chikusa-ku, Nagoya, Aichi 464-8602, Japan
- ⁶⁰ Department of Physics, The University of Hong Kong, Pokfulam, Hong Kong
- ⁶¹ Department of Astronomy and Astrophysics, Pennsylvania State University, University Park, PA 16802, USA
- ⁶² Université Grenoble Alpes, CNRS, IPAG, F-38000 Grenoble, France
- ⁶³ Center for Astrophysics—Harvard & Smithsonian, 60 Garden Street, Cambridge, MA 02138, USA
- ⁶⁴ Dipartimento di Fisica e Astronomia, Università degli Studi di Padova, Via Marzolo 8, I-35131 Padova, Italy
- ⁶⁵ Dipartimento di Fisica, Università degli Studi di Roma “Tor Vergata”, Via della Ricerca Scientifica 1, I-00133 Roma, Italy
- ⁶⁶ Department of Astronomy, University of Maryland, College Park, MD 20742, USA
- ⁶⁷ Anton Pannekoek Institute for Astronomy & GRAPPA, University of Amsterdam, Science Park 904, 1098 XH Amsterdam, The Netherlands
- ⁶⁸ Guangxi Key Laboratory for Relativistic Astrophysics, School of Physical Science and Technology, Guangxi University, Nanning 530004, People’s Republic of China

Received 2023 March 29; revised 2023 May 3; accepted 2023 May 3; published 2023 May 15

Abstract

We report the first $>99\%$ confidence detection of X-ray polarization in BL Lacertae. During a recent X-ray/ γ -ray outburst, a 287 ks observation (2022 November 27–30) was taken using the Imaging X-ray Polarimetry Explorer (IXPE), together with contemporaneous multiwavelength observations from the Neil Gehrels Swift observatory and XMM-Newton in soft X-rays (0.3–10 keV), NuSTAR in hard X-rays (3–70 keV), and optical polarization from the Calar Alto and Perkins Telescope observatories. Our contemporaneous X-ray data suggest that the IXPE energy band is at the crossover between the low- and high-frequency blazar emission humps. The source displays significant variability during the observation, and we measure polarization in three separate time bins. Contemporaneous X-ray spectra allow us to determine the relative contribution from each emission hump. We find $>99\%$ confidence X-ray polarization $\Pi_{2-4\text{keV}} = 21.7^{+5.6}_{-7.9}\%$ and electric vector polarization angle $\psi_{2-4\text{keV}} = -28.^{\circ}7 \pm 8.^{\circ}7$ in the time bin with highest estimated synchrotron flux contribution. We discuss possible implications of our observations, including previous IXPE BL Lacertae pointings, tentatively concluding that synchrotron self-Compton emission dominates over hadronic emission processes during the observed epochs.

Unified Astronomy Thesaurus concepts: [Astrophysical black holes \(98\)](#); [Black hole physics \(159\)](#); [Supermassive black holes \(1663\)](#); [Active galactic nuclei \(16\)](#); [Active galaxies \(17\)](#); [Jets \(870\)](#); [Galaxy jets \(601\)](#); [Relativistic jets \(1390\)](#); [Compact radiation sources \(289\)](#); [X-ray astronomy \(1810\)](#)

1. Introduction

Blazars are active galactic nuclei (AGNs) that launch collimated relativistic jets of plasma oriented within a few degrees from the observer’s line of sight (Blandford et al. 2019, and references therein). The Doppler-boosted jet emission dominates the observed spectral energy distribution (SED) that extends from radio to γ -rays and is characterized by two emission components. Blazars are often classified by the peak frequency of the low-energy (electron synchrotron radiation) component as low synchrotron peaked (LSP; $\nu_{\text{syn}} < 10^{14}$ Hz), intermediate synchrotron peaked (ISP; $10^{14} < \nu_{\text{syn}} < 10^{15}$ Hz), and high synchrotron

peaked (HSP; $\nu_{\text{syn}} > 10^{15}$ Hz; Abdo et al. 2010). Here we focus on ISPs and in particular BL Lacertae (BL Lac), whose recent γ -ray outburst (see Appendix C) briefly boosted its characteristic peak energies, moving it from the LSP into the ISP class.

In ISPs the peak of the low-energy component ranges from the near-IR through the UV bands. Thus, the 2–8 keV Imaging X-ray Polarimetry Explorer (IXPE) band may include substantial emission from the falling high-frequency tail of the leptonic synchrotron (Sy) spectrum emitted by the most efficiently accelerated electrons and positrons, by a related higher-frequency peak hadronic component (synchrotron emission from protons), or by flatter-spectrum synchrotron self-Compton (SSC) leptonic emission. Indeed, in leptonic models the IXPE band may lie in the U-shaped transition region from synchrotron to SSC emission (e.g., Peirson et al. 2022, their Figure 1). Since the polarization is expected to



Original content from this work may be used under the terms of the [Creative Commons Attribution 4.0 licence](#). Any further distribution of this work must maintain attribution to the author(s) and the title of the work, journal citation and DOI.

Table 1

Spectropolarimetric XSPEC Model Fit to the Joint NuSTAR, XMM-Newton, and IXPE Spectra Shown in Figure 1

Model Component	+2 Power laws
χ^2/dof	1102/1085
N_{H} (10^{21} cm 2)	3.10 ± 0.12
kT (keV)	0.345 ± 0.025
Γ_1	3.28 ± 0.100
Γ_2	1.62 ± 0.027
Π_1 (%)	27.6 ± 11.6
ψ_1 ($^\circ$)	-34.5 ± 11.6

Note. Γ : photon index, Π : polarization fraction, and ψ : EVPA. The polarization fraction of the second power-law component is fixed to zero.

differ between Sy and SSC, IXPE ISP observations can probe both radiation processes, and possibly the jet’s composition (Zhang & Böttcher 2013; Peirson et al. 2022). The latter is of particular interest, as blazars have been proposed as candidate sources of TeV neutrinos and ultrahigh-energy cosmic rays (UHECRs), which would require a significant hadronic component in some blazar jets (Gao et al. 2019). The possible 3σ association of ISP blazar TXS 0506+056 with the neutrino IceCube-170922A event motivates this connection (Kintscher et al. 2017; Icecube Collaboration et al. 2018). However, the peculiar γ -ray behavior of TXS 0506+056 and the $\sim 40\%$ probability of an atmospheric origin of the neutrino challenges the association. Current blazar models that include neutrino emission assume either lepto-hadronic X-ray emission (e.g., Cerruti et al. 2019) or subdominant hadronic components where the proton emission only dominates the SED in the transition region where the leptonic component is at a minimum level (e.g., Gao et al. 2019). These factors highlight the importance of distinguishing between leptonic and hadronic emission in an ISP blazar when it comes to X-ray polarization measurements with IXPE.

BL Lacertae is among the few LSP or ISP blazars detected at ≥ 0.1 TeV (very high energy; VHE) γ -ray energies, and is the 14th brightest AGN at GeV energies in the Fermi 4LAC catalog (Ajello et al. 2020). It is a rapidly variable VHE source on timescales as short as < 1 hr (Albert et al. 2007; Arlen et al. 2013). Moreover, BL Lacertae has been the focus of a large number of multiwavelength and polarization studies (e.g., Raiteri et al. 2013; Blinov et al. 2015; Weaver et al. 2020; Casadio et al. 2021). Because of this blazar’s strong variability, the interpretation of its SED requires simultaneous observations.

In this paper, we report the first $>99\%$ confidence detection of X-ray polarization in BL Lacertae, with redshift $z = 0.0686$ (Vermeulen et al. 1995) and synchrotron peak frequency $\nu_{\text{syn}} = 1.98 \times 10^{14}$ Hz (Chen 2014). Although BL Lacertae is typically classified as an LSP, where the hard secondary SED component dominates the soft X-ray band, its recent outburst both softened and brightened its X-ray spectrum. The soft X-ray flux and photon index are highly variable, but typically $< 2 \times 10^{-11}$ erg cm 2 s $^{-1}$ and < 2 , respectively (e.g., Wehrle et al. 2016; Giommi et al. 2021; Middei et al. 2022; Sahakyan & Giommi 2022). However, during the recent flare Swift-XRT found flux $F_{2-8\text{keV}} = (2.77 \pm 0.21) \times 10^{-11}$ erg cm 2 s $^{-1}$ and photon index = 2.10 ± 0.09 on 2022 November 12, which suggests a significant contribution from the synchrotron component.

In Section 2 we describe the X-ray, optical, and radio polarization observations and data reduction. We discuss our findings in the context of multiwavelength observations in Section 3. Further analysis details can be found in Appendices B and C.

2. Data Analysis

BL Lacertae was observed by IXPE with an exposure time of 287 ks on 2022 November 27–30 (MJD 59910.58–59913.90). IXPE, launched on 2021 December 9, is a joint mission of NASA and the Italian Space Agency (Agenzia Spaziale Italiana, ASI). A description of the instrument is given by Weisskopf et al. (2022). At the $\sim 30''$ angular resolution of IXPE, BL Lacertae is a point-like source. Quasi simultaneously, BL Lacertae was observed in the hard and soft X-ray bands with NuSTAR (MJD 59911.87–59912.31), XMM-Newton (MJD 59910.27–59910.39), and Swift-XRT (MJD 59910.16, 59911.89, 59912.22, and 59913.43), in linear polarization in the optical *BVRi* bands with Calar Alto, the Nordic Optical Telescope (NOT), the 1.8 m Perkins Telescope of Boston University, and the Sierra Nevada Observatory, and at millimeter wavelengths by the Institut de Radioastronomie Millimétrique 30 m Telescope (IRAM-30m) and Submillimeter Array (SMA). Additional low-frequency radio observations were performed with the Effelsberg 100 m telescope (4.85–10.45 GHz) and Korean very long baseline interferometry (VLBI) Network (KVN; 22–123 GHz). Appendices A and C detail the data reduction of these multiwavelength observations. The IXPE data were calibrated and reduced following standard procedures within the *ixpeobssim* pipeline⁶⁹ (Baldini et al. 2022).

We begin by measuring the model-independent, constant polarization parameters for the full IXPE observation using *ixpeobssim*’s PCUBE algorithm, finding 99% upper limits on the polarization fraction of 14.3% (2–8 keV) and 19.8% (2–4 keV).

To characterize the contribution of the two emission components in the IXPE 2–8 keV band and identify a fiducial spectral model, we first attempt to fit the broadband X-ray spectrum averaged over the whole observation, including XMM-Newton 0.3–10 keV and NuSTAR 3–80 keV data. A simple absorbed power-law model is inadequate, with $\chi^2/\text{dof} = 1898/1087$. We find the sum of two absorbed power laws best reproduces the observations, as measured by χ^2 per degree of freedom (dof), Table 1. XMM-Newton measurements below 1 keV require an additional soft spectral component, probably from a hot diffuse plasma, as noted for BL Lacertae by Middei et al. (2022); we thus add an unpolarized apec component in XSPEC. The temperature and normalization of this apec component are free parameters in the fit. The best-fit absorption column density, $N_{\text{H}} = 3.1 \pm 0.12 \times 10^{21}$ cm $^{-2}$, is consistent with values from previous studies (e.g., $N_{\text{H}} = 2.8 \pm 0.05 \times 10^{21}$ cm $^{-2}$; Weaver et al. 2020). Figure 1 shows the results of the double power-law fit, including the individual power-law and apec components. We note that the soft power-law component comprises 36.7% (2–4 keV) or 26.1% (2–8 keV) of the total flux.

By extending to a spectropolarimetric fit and restricting the softer power law to have constant linear polarization, while

⁶⁹ <https://agenda.infn.it/event/15643/contributions/30820/attachments/21780/24810/ixpeobssim.pdf>.

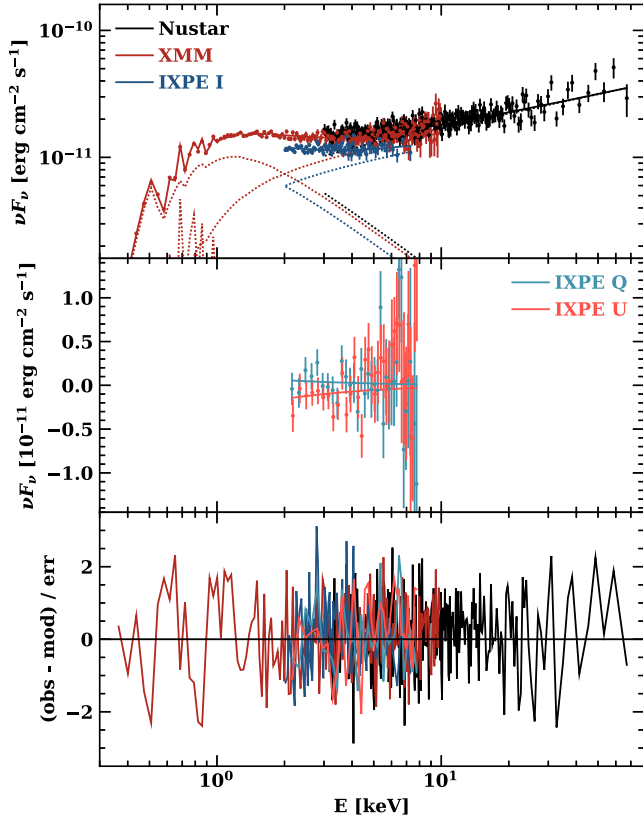


Figure 1. Quasi-simultaneous X-ray spectra during the IXPE observation. The fitted model is the sum of two absorbed power laws and an apec component. Dotted lines in the top panel show the individual power-law and apec components. The middle panel shows the polarized spectra with constant polarization for the low-energy component; the high-energy component has fixed polarization degree = 0. The significance of the spectral fit residuals is shown in the bottom panel.

assuming that the harder power law is unpolarized, we find $\Pi_X = 27.6\% \pm 11.6\%$ (with $\Pi_X < 57.6\%$ at 99% confidence) and $\psi_X = -34.^\circ 5 \pm 11.^\circ 6$. We do not consider this a significant detection, since it does not meet our 99% confidence of nonzero polarization requirement. We discuss the rationale for assuming an unpolarized high-energy component in Section 3. Allowing both power laws to have independent, constant polarization results in high, nearly orthogonal values, which cancel the net polarization over most of the spectrum; these values are poorly constrained owing to the poor statistics.

2.1. Time Variability

The null result is based on the assumption of constant polarization with time of both power-law spectral components. However, the source is clearly variable during the present IXPE epoch, which may affect the derived polarizations. To assess this, we split the observation into three equal time bins based on the IXPE count spectrum and optical observations. We also analyze the data over two energy bins, measuring separately the low- (2–4 keV) and full-energy (2–8 keV) ranges. To check whether the polarization degree and electric vector position angle (EVPA) vary with energy, supporting a multicomponent interpretation, we make model-independent measurements of constant polarization in each time and energy bin, as shown Figure 2.

XMM-Newton and NuSTAR observations straddle the first time bin, and three short ~ 1 ks Swift-XRT exposures are

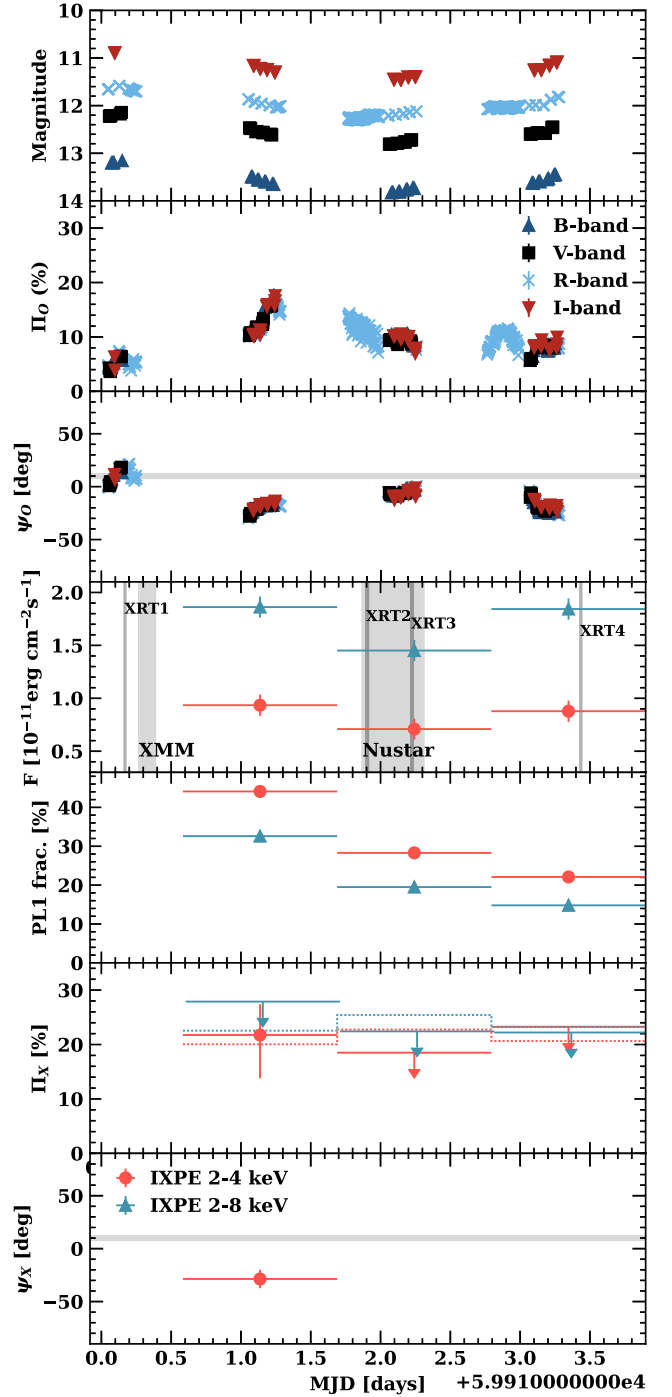


Figure 2. Light curves, polarization fractions, and EVPAs in the optical (top three panels) and X-ray (bottom three panels) bands. The X-ray soft power flux contribution fraction is shown in the middle panel. In the X-ray panels, the data are split into two energy bins and three equal time bins. The times of observations from satellites other than IXPE are indicated in the flux panel. Errors are 68.3% (1σ) confidence intervals and upper limits are 99% confidence. Shaded horizontal regions in EVPA panels represent the jet axis projection on the plane of the sky (Weaver et al. 2022). Dotted lines in the X-ray polarization-fraction panel represent the MDP99 level for each bin individually. For the X-ray polarization measurements, only the first time bin at 2–4 keV exceeds MDP99.

available, two within the second time bin and the other in the final time bin. To assess the contribution of the individual power-law components to each time bin, we fit the absorbed sum of a double power-law model (Table 1) separately to each

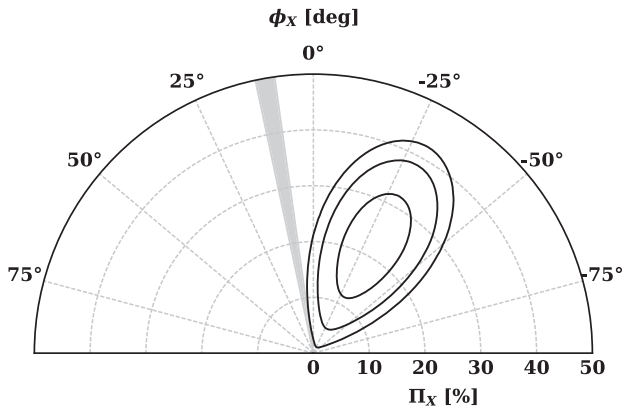


Figure 3. Polarization fraction and EVPA confidence levels (68%, 95%, and 99%) for the first time bin over the 2–4 keV energy range, Figure 2. Gray shaded region represents the VLBI-determined jet axis projection on the plane of the sky (Weaver et al. 2022).

appropriate set of IXPE plus Swift-XRT time-binned spectra, fixing the photon indices Γ_1 and Γ_2 to their NuSTAR plus XMM-Newton fitted values. This allows the power-law normalizations to vary in time while their slopes remain fixed. Estimated fractions of the soft power-law (synchrotron) contribution for each time and energy bin are displayed in Figure 2. While the similar variations of the fluxes in the two energy bins (Figure 2) show that both power laws vary together (as expected for synchrotron and Compton components), we find that the soft-component contribution is largest in the first time bin, as might be expected from observations at the high-energy tail of a cooling synchrotron flare.

Interestingly, in the low-energy channel within the first time bin, where our spectral fits indicate that the soft component contributes the maximum flux, we detect linear polarization exceeding minimum detectable polarization at 99% confidence (MDP99), as displayed in Figure 3. When considered as a single measurement, we find 99.3% confidence in nonzero polarization. Considering all three binned 2–4 keV polarization measurements jointly we find a 98.4% confidence in nonzero polarization. As noted previously, we do not exceed the 99% threshold over the full time interval.

We have attempted full spectropolarimetric double power-law fits to each time bin as in Figure 1, but none produced a high-significance detection for the soft power-law component. Instead, we have used these fits to estimate the lower-energy power-law (synchrotron) contribution fractions in Figure 2. The results for all such fits are detailed in Appendix B.

3. Discussion and Conclusions

In order to fit our XMM-Newton and NuSTAR spectra, (Figure 1), we find that a two-component spectrum is required for BL Lacertae. A power-law fit with low-energy photon index $\Gamma_1 = 3.28$ and high-energy value $\Gamma_2 = 1.62$, with equal flux at 2 keV, is statistically preferred over a simple power law. Our polarization results thus probe the crossover region.

Pure leptonic models predict a significant decrement in polarization of the hard (Compton) component relative to the optical synchrotron value, with $\Pi_{\text{SSC}}/\Pi_{\text{Sy}} \approx 0.3$ (Krawczynski 2012; Peirson & Romani 2019). When the high-energy tail of the synchrotron emission reaches into the IXPE band, we might expect the soft-component polarization even to exceed

the optical value if the X-ray emission arises from a region of a more highly ordered magnetic field.

One possibility is that the X-ray synchrotron emission occurs mainly in the acceleration and collimation zone of the jet, where the magnetic field is expected to have a well-ordered helical geometry (e.g., Vlahakis & Königl 2004), as inferred previously in BL Lacertae (Marscher et al. 2008). Alternatively, the emission could take place in a region of the jet with a turbulent magnetic field, with the acceleration of particles occurring only within a small volume, for example by magnetic reconnection. Since X-ray synchrotron radiation requires extremely high-energy electrons that are subject to strong radiative energy losses, the X-ray emission would be confined to locations close to the site of particle acceleration, while lower-frequency emission from lower-energy electrons, which can travel farther from the acceleration site before their fractional energy loss becomes high, would occur over a larger volume. In a turbulent magnetic field, the net field is more ordered (but randomly oriented) over smaller volumes, hence the polarization is higher (see, e.g., Marscher 2014; Peirson & Romani 2018, for discussions and estimates). The random value of ψ agrees with our finding that the observed EVPA does not appear related to the direction of the jet.

If the turbulent plasma encounters a shock, the magnetic field becomes partially aligned with the shock front (e.g., Hughes et al. 1985; Marscher 2014; Tavecchio et al. 2018), at which X-ray-emitting particles can be accelerated. By the same argument as above, the synchrotron X-ray polarization should then be higher than at longer wavelengths, but instead of a random orientation of the EVPA, ψ should be oriented along the jet direction, contrary to the observations of BL Lacertae presented here.

During a synchrotron X-ray flare, the more highly polarized synchrotron component contributes more to the X-ray spectrum at lower X-ray energies than does the flatter-spectrum Compton component. As this steep-spectrum component fades across the IXPE band, the lower Compton polarization should dominate at higher energies. Although the EVPAs measured at the synchrotron peak and SSC peak frequencies are expected to be correlated (Peirson & Romani 2019), turbulence and energy-dependent emission volumes can cause differences.

To constrain best the soft-component polarization we assume that the high-energy power-law component is negligibly polarized, as the logical approximation of the expected polarization decrease noted above. The polarization $\Pi_X = 27.6\% \pm 11.6\%$ measured over all IXPE times and energies, while a $>2\sigma$ detection, does not reach the threshold for high significance. However, noting that the soft component varies in strength, we find that a time and energy bin analysis allows a significant $\Pi_X = 21.7_{-7.9}^{+5.6}\%$ detection at low energies in the first time bin, when the spectral analysis indicates that the soft component accounts for the largest fraction of the total flux. Note that this polarization is substantially higher than the simultaneous optical polarization $\Pi_O = 13.1\% \pm 2.4\%$ for the same time bin. Both the optical and X-ray EVPA are at $\sim 40^\circ$ to the projection of BL Lacertae’s jet axis on the plane of the sky at 43 GHz (Weaver et al. 2022).

Even the first time/energy bin is diluted by the high-energy component. Under the assumption of relatively constant photon indices at the XMM-Newton and NuSTAR values, the high-energy component still comprises 56% of the flux in this 2–4 keV time bin (Figure 2). If the component is unpolarized,

correction for this flux implies $\Pi_{\text{Sy}} = 21.7\% / (1 - 0.56) \approx 49\%$ for the soft component; if the high-energy component corresponds to Compton scattering, polarized at $\sim 0.3 \times$ the synchrotron value with approximately the same EVPA, the polarization of the low-energy component is $\Pi_{\text{Sy}} = 21.7\% / ((1 - 0.56) + 0.3 \times 0.56) \approx 36\%$. These polarization degrees are consistent with the upper limit provided by the double power-law spectral fit in Table 4 of the Appendix. These large values dramatically exceed the optical polarization, arguing that we are probing the high-frequency end of the synchrotron component, which fades during our observation window.

Two previous IXPE observations of BL Lacertae (Middei et al. 2023), which occurred during a low state, where the X-ray spectrum was apparently dominated by SSC, produced upper limits on Π_X that were significantly below the simultaneous optical polarization. However, in the data from the third epoch presented here, even the total (time and energy) averaged IXPE polarization signal is comparable to the optical values. After correction for hard-component contamination, the soft component substantially exceeds the optical polarization degree.

Other scenarios have different polarization signatures. In simple single-zone leptohadronic models, the polarization should be similar across the transition region (Figure 1). Synchrotron emission from primary leptons producing the low-energy hump yields to higher-energy synchrotron radiation from protons and secondary leptons produced in $p\gamma$ cascades (Zhang & Böttcher 2013), all in the same magnetic field environment. As noted above, in more realistic jet models, turbulent magnetic fields, differential cooling times (Marscher et al. 2010), and relativistic boosting (Peirson & Romani 2019) cause a significant increase in polarization and changes in EVPA as one approaches the quasi-exponential cutoff of the low-energy peak, where only the highest-energy electrons from the most efficient particle acceleration zones contribute synchrotron emission. If a hadronic emission component becomes dominant above this energy, it should be averaged over the lower-energy particle population typical of particle acceleration in the jet, and thus should display polarization similar to that of the primary (optical) synchrotron peak. In models including hadronic synchrotron emission, we expect the polarization fraction at the upper end of the transition region to meet or exceed the optical value.

Our past measurements of $\Pi_X < \Pi_O$ (Middei et al. 2023) and the persistent low polarization at the upper end of the IXPE band therefore argues against a leptohadronic emission model. Furthermore, the detection of total polarization at low energies, with $\Pi_{2-4 \text{ keV}} \gg \Pi_O$, indicates that we are sampling the upper cutoff of the synchrotron spectrum. This is even more striking after correcting for dilution by the hard, weakly polarized component. The decreasing relative flux of the soft component and the resulting loss of detection of polarization are consistent with the tail end of a jet flare, as suggested by the γ -ray and X-ray light curves.

While these results provide tentative evidence for a fully leptonic emission model in BL Lacertae at our IXPE observation epoch, variability allows significant hadronic emission at other times. Blazars are particularly variable in polarization (Blinov et al. 2018), and broadband or long-exposure measurements can make polarization results difficult to interpret properly (Kiehlmann et al. 2021; Peirson et al. 2022). Thus, repeated polarization measurements of blazars, with attendant contemporaneous multiwavelength intensity and

polarization observations, are needed to explore blazar emission fully. Most interesting would be measurements during flares associated with neutrino events. With the plausible neutrino connection, and the ability to probe the critical Sy/SSC transition regions, BL Lacertae and other ISPs will be prime targets for such studies.

The Imaging X-ray Polarimetry Explorer (IXPE) is a joint US and Italian mission. The US contribution is supported by the National Aeronautics and Space Administration (NASA) and led and managed by its Marshall Space Flight Center (MSFC), with industry partner Ball Aerospace (contract NNM15AA18C). The Italian contribution is supported by the Italian Space Agency (Agenzia Spaziale Italiana, ASI) through contract ASI-OHBI-2017-12-I.0, agreements ASI-INAF-2017-12-H0 and ASI-INFN-2017.13-H0, and its Space Science Data Center (SSDC) with agreements ASI-INAF-2022-14-HH.0 and ASI-INFN 2021-43-HH.0, and by the Istituto Nazionale di Astrofisica (INAF) and the Istituto Nazionale di Fisica Nucleare (INFN) in Italy. This research used data products provided by the IXPE Team (MSFC, SSDC, INAF, and INFN) and distributed with additional software tools by the High-Energy Astrophysics Science Archive Research Center (HEASARC), at NASA Goddard Space Flight Center (GSFC). Funding for this work was provided in part by contract 80MSFC17C0012 from the MSFC to MIT in support of the IXPE project. Support for this work was provided in part by the NASA through the Smithsonian Astrophysical Observatory (SAO) contract SV3-73016 to MIT for support of the Chandra X-Ray Center (CXC), which is operated by SAO for and on behalf of NASA under contract NAS8-03060. The IAA-CSIC coauthors acknowledge financial support from the Spanish “Ministerio de Ciencia e Innovación” (MCIN/AEI/10.13039/501100011033) through the Center of Excellence Severo Ochoa award for the Instituto de Astrofísica de Andalucía-CSIC (CEX2021-001131-S), and through grants PID2019-107847RB-C44 and PID2022-139117NB-C44. Some of the data are based on observations collected at the Observatorio de Sierra Nevada, owned and operated by the Instituto de Astrofísica de Andalucía (IAA-CSIC). Further data are based on observations collected at the Centro Astronómico Hispano-Alemán (CAHA), operated jointly by Junta de Andalucía and Consejo Superior de Investigaciones Científicas (IAA-CSIC). The POLAMI observations were carried out at the IRAM 30 m Telescope. I.R.A.M. is supported by INSU/CNRS (France), MPG (Germany), and IGN (Spain). The Submillimetre Array is a joint project between the Smithsonian Astrophysical Observatory and the Academia Sinica Institute of Astronomy and Astrophysics and is funded by the Smithsonian Institution and the Academia Sinica. Maunakea, the location of the SMA, is a culturally important site for the indigenous Hawaiian people; we are privileged to study the cosmos from its summit. The data in this study include observations made with the Nordic Optical Telescope, owned in collaboration by the University of Turku and Aarhus University, and operated jointly by Aarhus University, the University of Turku, and the University of Oslo, representing Denmark, Finland, and Norway, the University of Iceland, and Stockholm University at the Observatorio del Roque de los Muchachos, La Palma, Spain, of the Instituto de Astrofísica de Canarias. The data presented here were obtained in part with ALFOSC, which is provided by the Instituto de Astrofísica de Andalucía (IAA)

under a joint agreement with the University of Copenhagen and NOT. E.L. was supported by Academy of Finland projects 317636 and 320045. We acknowledge funding to support our NOT observations from the Finnish Centre for Astronomy with ESO (FINCA), University of Turku, Finland (Academy of Finland grant nr 306531). The research at Boston University was supported in part by National Science Foundation grant AST-2108622, NASA Fermi Guest Investigator grants 80NSSC21K1917 and 80NSSC22K1571, and NASA Swift Guest Investigator grant 80NSSC22K0537. This study used observations conducted with the 1.8 m Perkins Telescope Observatory (PTO) in Arizona (USA), which is owned and operated by Boston University. The above study is based in part on observations obtained with XMM-Newton, an ESA science mission with instruments and contributions directly funded by ESA Member States and NASA. We are grateful to the NuSTAR team for approving our DDT request. This work was supported under NASA contract No. NNG08FD60C, and made use of data from the NuSTAR mission, a project led by the California Institute of Technology, managed by the Jet Propulsion Laboratory, and funded by the NASA. This research has made use of the NuSTAR Data Analysis Software (NuSTARDAS) jointly developed by the ASI Science Data Center (ASDC, Italy) and the California Institute of Technology (USA). This work was supported by JST, the establishment of university fellowships toward the creation of science technology innovation, grant No. JPMJFS2129. This work was supported by Japan Society for the Promotion of Science (JSPS) KAKENHI grant No. JP21H01137. This work was also partially supported by Optical and Near-Infrared Astronomy Inter-University Cooperation Program from the Ministry of Education, Culture, Sports, Science, and Technology (MEXT) of Japan. We are grateful to the observation and operating members of Kanata Telescope. M. N. acknowledges the support by NASA under award number 80GSFC21M0002. C.C. acknowledges support by the ERC under the Horizon ERC Grants 2021 program under grant agreement no. 101040021. S.K., S.-S.L., W.Y.C., S.-H.K., and H.-W.J. were supported by the National Research Foundation of Korea (NRF) grant funded by the Korea government (MIST; 2020R1A2C2009003). The KVN is a facility operated by the Korea Astronomy and Space Science Institute. The KVN operations are supported by KREONET (Korea Research Environment Open NETwork), which is managed and operated by KISTI (Korea Institute of Science and Technology Information). Partly based on observations with the 100 m telescope of the MPIfR (Max-Planck-Institut für Radioastronomie) at Effelsberg. Observations with the 100 m radio telescope at Effelsberg have received funding from the European Union’s Horizon 2020 research and innovation program under grant agreement No 101004719 (ORP). A.L.P. acknowledges support from NASA FINESST grant 80NSSC19K1407 and the Stanford Data Science Scholars program.

Facilities: Calar Alto, Effelsberg-100 m, IRAM-30 m, IXPE, Kanata, KVN, Nordic Optical Telescope, NuSTAR, Perkins, SMA, XMM-Newton, and Swift.

Appendix A X-Ray Observations

Between 2022 November 27–30, BL Lacertae was observed quasi simultaneously with IXPE, NuSTAR, and XMM-Newton; see Table 2. For the IXPE data, the cleaned event files and the associated science products were obtained using a dedicated pipeline relying on the Ftools software package and adopting the latest calibration data files from IXPE (CALDB 20211118). The source regions for each of the three detector units (DUs) were then selected via an iterative process aimed at maximizing the signal-to-noise ratio (S/N) over the IXPE standard energy range of 2–8 keV. In particular, we used circular regions with radius 50'' for all three DUs and annulus regions of size 100''–300'' for the background spectra in Stokes parameters I , Q , and U .

To improve the polarimetric sensitivity, we applied a background rejection strategy (Xie et al. 2021; Di Marco et al. 2023). The method refines the sensitivity by applying energy-dependent cuts on photoelectron tracks from the level 1 data. This method substantially decreases the background event rate, which are triggered by electrons, positrons, muons, or protons either directly impinging upon the detector or created by high-energy interactions in the surrounding satellite structures. The cuts employ (1) the number of pixels: the size of the track region of interest (NUM_PIX); (2) energy fraction: the fraction of the event energy in the track (EVT_FRA); and (3) border pixels: the number of activated pixels along the boundary of the detector (NUM_TRK). Here we eliminated the events that do not satisfy the X-ray photon criteria of A. Di Marco et al. (2023, submitted). Using the point source as a monitor, we rejected $\sim 30\%$ of the diffuse background, with little impact on the source events. For the IXPE spectropolarization analysis, a constant energy binning of 4×0.05 keV PI channels per bin was used for Q and U ; we required 30 counts per bin for the intensity spectra.

The XMM-Newton spectra were produced with standard SAS routines and the latest calibration files. The source spectrum was extracted from a circular (radius = 40'') aperture, while the background spectrum was extracted from a blank region on the Epic-pn CCD camera from a circular region of the same size. The resulting spectrum was regrouped to include at least 30 counts in each bin and to avoid $>3\times$ oversampling of the spectral resolution. The NuSTAR data were calibrated and cleaned with the NuSTAR Data Analysis Software (NuSTARDAS7), and employed the nuproducts pipeline using the latest calibration database (v. 20220302). The source spectrum was extracted from a circular radius of 70'' aperture; a surrounding 270''–370'' annulus provided the background.

Swift-XRT exposures were obtained in the context of a monitoring campaign tracking the BL Lacertae flux level before, during, and after the IXPE pointing. Scientific products from the Swift-XRT exposures were derived by using the facilities provided by the Space Science Data Center (SSDC8) of the Italian Space Agency (ASI). In particular, the source

Table 2
Major Quasi-simultaneous X-Ray Observations Related to the 2022 November 27 IXPE Pointing of BL Lacertae

Observatory	Start Time	MJD Range	ObsID	Exposure (ks)
NuSTAR	2022-11-28 20:51:09	59911.87–59912.31	90801633002	38.1
XMM-Newton	2022-11-27 06:26:53	59910.27–59910.39	0902111801	10.1
IXPE	2022-11-27 14:01:15	59910.58–59913.90	02005901	286.4

Table 3
Swift-XRT Exposures in the Vicinity of the IXPE Pointing of BL Lacertae

Start Time	MJD	ObsID	Exposure (s)	Flux (2–8 keV) (10^{-11} erg cm^{-2} s^{-1})	Γ
2022-11-27 03:56:36	59910.16	00096990016	834	0.827	2.24
2022-11-28 21:30:17	59911.89	00089562001	1474	1.57	1.94
2022-11-29 05:13:35	59912.21	00096990017	826	2.04	2.13
2022-11-30 10:19:01	59913.42	00096990018	895	2.22	1.78
2022-12-01 02:07:36	59914.09	00096990019	849	1.97	1.87

Note. Figure 4 displays the exposures superimposed on the IXPE light curve. To measure the flux and Γ , single absorbed power laws were fit to the full XRT 0.3–10 keV range.

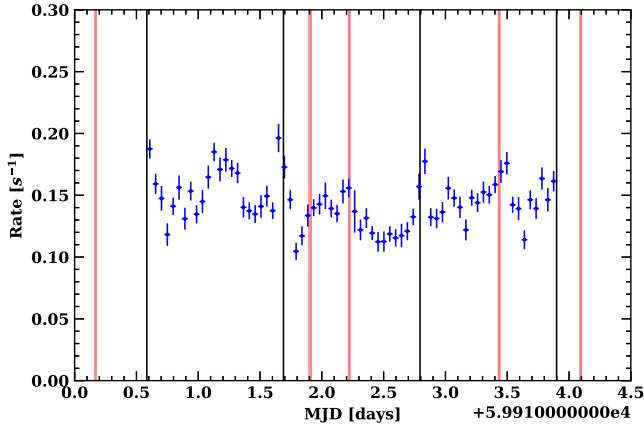


Figure 4. IXPE light curve. Black lines are three equal time bin separators; red shaded regions indicate XRT exposures.

spectra were extracted from a source-centered $47''$ radius aperture, with a $120''$ – $150''$ concentric annulus providing a background spectrum. The events were grouped to include at least 25 counts in each spectral bin. We modeled each of the four XRT spectra as a simple power law with Galactic photoelectric absorption. We report the 2–8 keV fluxes and the inferred photon indices in Table 3, with the exposures superimposed on the IXPE light curve in Figure 4. The softest spectrum corresponds to the first IXPE time bin, shown in Figure 2, for which the highest polarization is measured. As discussed in Section 3, softer spectra represent a higher synchrotron fraction.

Appendix B Time-resolved Spectropolarimetric Analysis

We use XSPEC to perform spectropolarimetric analyses on the entire IXPE observation, including the NuSTAR and XMM-Newton spectra, and each of the three IXPE time bins defined in the main text; see Figure 2. The analysis of the entire observation is discussed in the main text (Figure 1, Table 1), where we find that an absorbed sum of two power laws with an apec component,

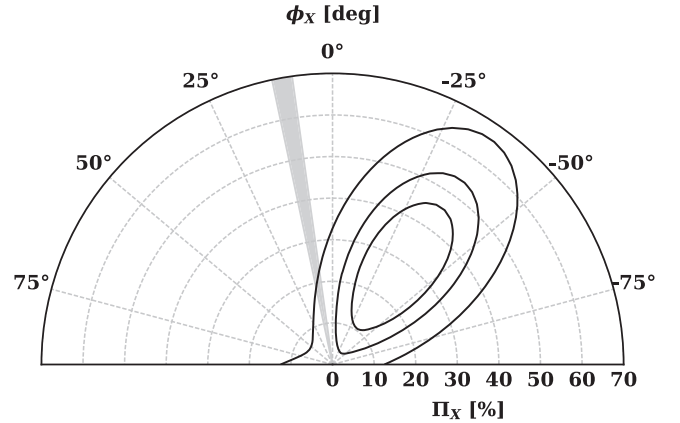


Figure 5. Polarization fraction and EVPA confidence levels (68%, 95%, 99%) for the low-energy power law in Figure 1. Gray shaded region represents the VLBI-determined jet axis projection on the plane of the sky (Weaver et al. 2022).

$$\text{constant} * \text{tbAbs} * (\text{polconst} * \text{powerlaw} + \text{polconst} * (\text{apec} + \text{powerlaw}))$$

is preferred according to XSPEC model fitting. Here we fix polarization degree of both the high-energy power law and apec to zero. Figure 5 displays a contour plot with the polarization measurement of the low-energy power law for the full IXPE observation fit, as displayed in Figure 1. We note that fixing the polarization degree of the high-energy power-law to $0.3 \times$ the synchrotron, as expected in a leptonic model, does not improve the significance of the fit.

In the case of the three IXPE time bins, we use the same model as above, but with photon indices and apec temperature (Γ_1 , Γ_2 , kT) fixed to the values found in the full observation fit; see Table 1. Hence, only the power-law normalization constants and low-energy power-law polarization are determined by the fits. We fit this model to the time-binned IXPE spectra along with the appropriate XRT observation(s); see Figure 2. The first time bin does not have a simultaneous XRT observation, and the second time bin has two (XRT2 and XRT3). Table 4 and Figure 6 give the results of these fits. We are able to determine the relative flux contribution of the low-

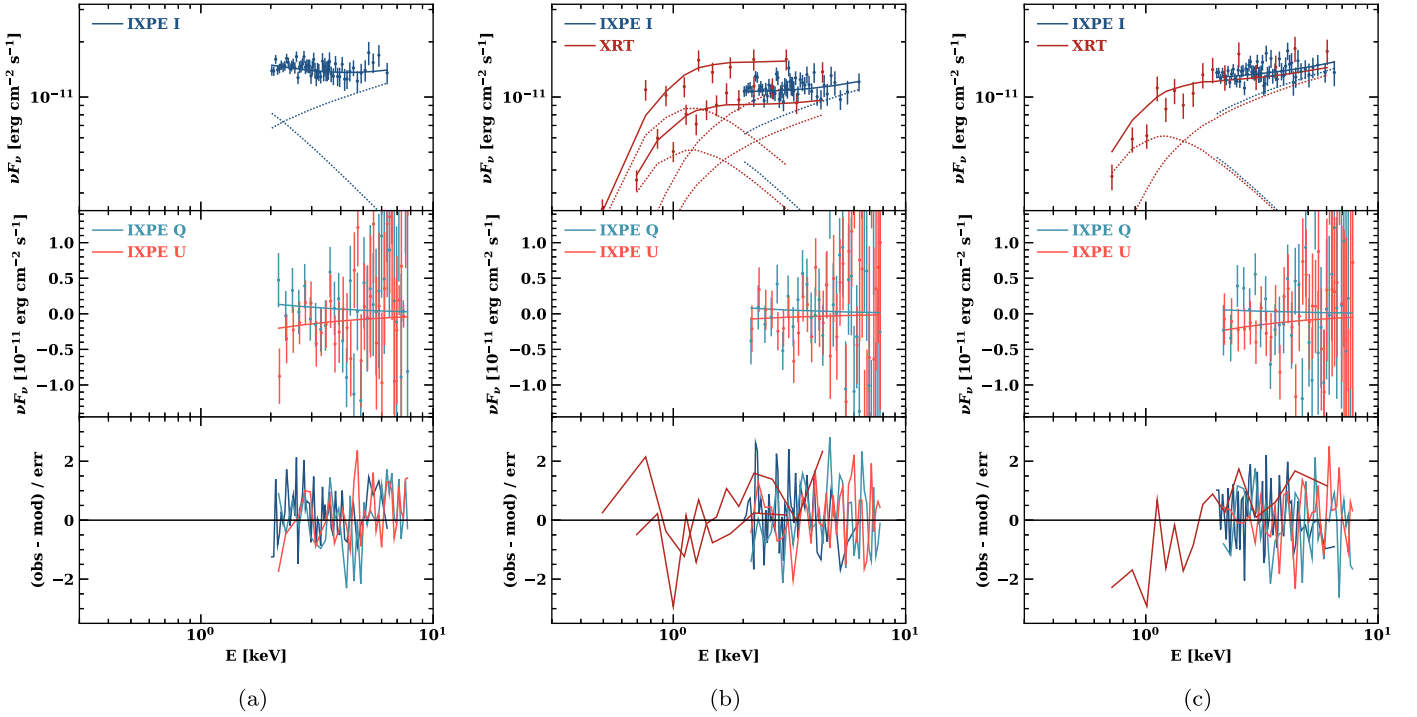


Figure 6. (a) Absorbed sum of two power laws with apec fit to first IXPE time bin. The photon indices and apec temperature are fixed to the values in Table 1. The high-energy power-law polarization is fixed to zero. (b) Second IXPE time bin with XRT2 and XRT3 observations. (c) Third IXPE time bin with XRT4 observation.

Table 4

Sum of Two Power-law Spectropolarimetric XSPEC Model Fits to the Time-binned IXPE and Swift-XRT Spectra Shown in Figure 1

Model Component	Time Bin		
	1	2	3
χ^2/dof	393/386	461/382	406/392
PL1 norm	$(4.33 \pm 0.32) \times 10^{-3}$	$(2.28 \pm 0.23) \times 10^{-3}$	$(2.44 \pm 0.26) \times 10^{-3}$
PL2 norm	$(1.14 \pm 0.062) \times 10^{-3}$	$(1.00 \pm 0.49) \times 10^{-3}$	$(1.31 \pm 0.056) \times 10^{-3}$
Π_1 [%]	<69.5	<89.9	<98.0
ψ_1 [°]	n/a	n/a	n/a

Note. Photon indices Γ_1 , Γ_2 , apec temperature kT , and N_H are fixed to their full-spectrum fit values; see Table 1. High-energy power-law polarization is fixed to zero. Π : polarization fraction and ψ : EVPA. Relative power-law normalizations in each time bin dictate the soft power-law fractions in Figure 1.

energy power law in Figure 2, which correspond to the power-law normalization constants at 1 keV.

Appendix C Multiwavelength Observations

During the IXPE observation, BL Lacertae was contemporaneously observed in polarization by different telescopes at radio, millimeter, and optical wavelengths. Low-frequency radio observations (4.85–10.45 GHz) were performed using the Effelsberg 100 m telescope through the QUIVER program (Monitoring the Stokes Q , U , I , and V Emission of AGN jets in Radio) on 2022 December 1 (MJD 59914.94424), and KVN *22–129 GHz) on 2022 November 30 (MJD 59913.6). Millimeter-wave observations were performed by IRAM-30m on 2022 November 28 (MJD 59911.5717) at 1.3 mm (228.93 GHz) and 3.5 mm (86.24 GHz), and by SMA at 1.3 mm (225.538 GHz) on 2022 December 1 (MJD 59914.0).

The QUIVER observations are performed at several radio bands (depending on receiver availability and weather

conditions) from 2.6 to 44 GHz (11 cm to 7 mm wavelength). The receivers are equipped with two orthogonally polarized feeds (either circular or linear) that can deliver polarimetric observables using either native polarimeters or by connecting the SpecPol spectropolarimetric backend. Instrumental polarization is calibrated using observations of both polarized and unpolarized calibrators performed in each session and removed from the data (e.g., Kraus et al. 2003; Myserlis et al. 2018). The polarized intensity, position angle, and polarization percentage were derived from the Stokes I , Q , and U cross-scans. For frequencies <10 GHz, we find polarization degree $\Pi_R \sim 5\%$ with polarization angle ψ_R between 148° and 188° . The radio spectrum obtained between 2.6 and 43 GHz shows a smooth increase in flux toward higher frequencies, corresponding to a (hard) radio spectrum with spectral index of $a = +0.25$ ($S \propto \nu^a$). We find a continuous rotation of the polarization angle between 4.85 and 10.45 GHz that suggests the presence of a Faraday screen with a rotation measure (RM) ~ -230 rad m^{-2} .

The KVN observations were performed with two 21 m antennas (KVN Yonsei and Tamna) in single-dish mode. The

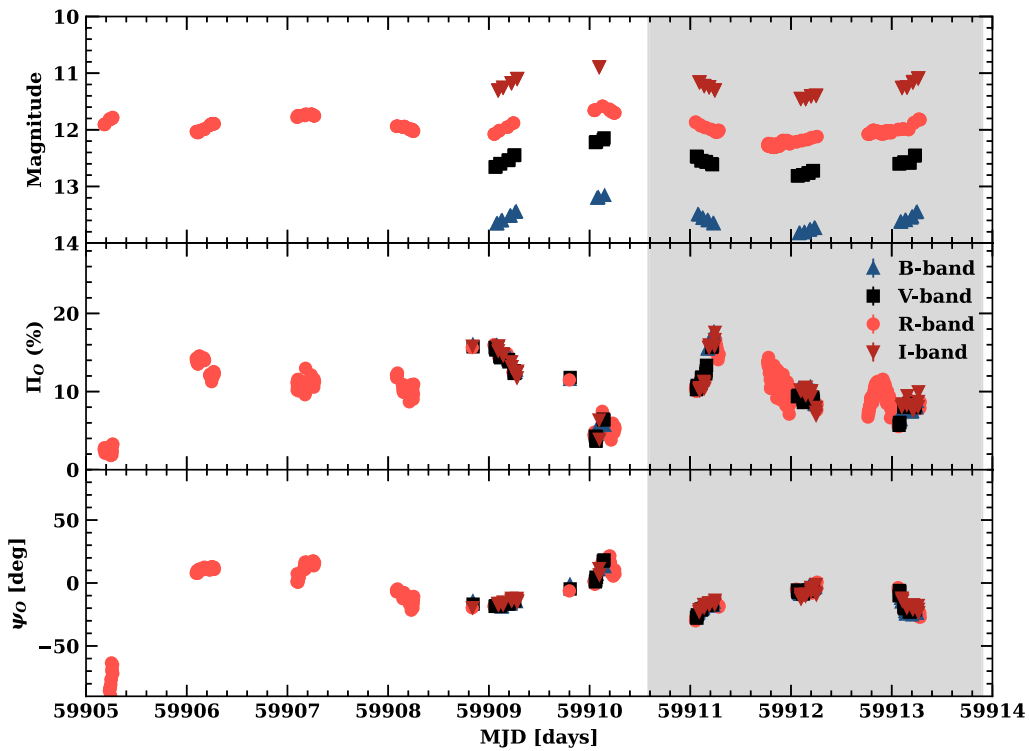


Figure 7. Optical *BVRI* observations of BL Lacertae before and during the 2022 November 27–30 IXPE pointing, showing brightness in magnitudes (top panel), polarization degree (middle panel), and polarization position angle (bottom panel). The duration of the IXPE observation is marked by the gray shaded area.

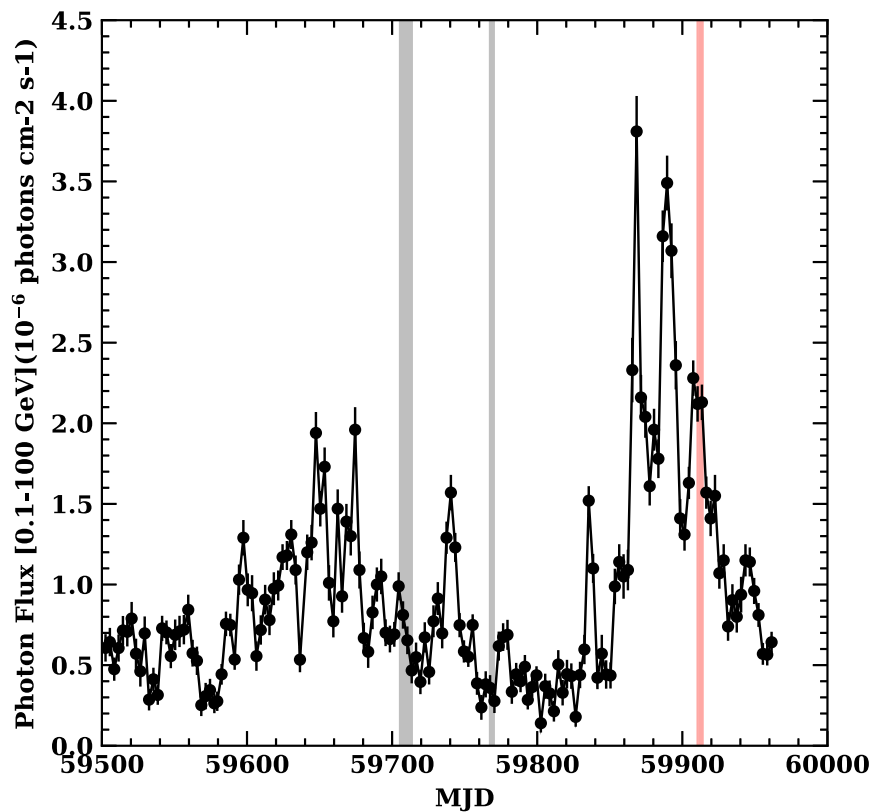


Figure 8. Fermi-LAT three day cadence light curve, showing the outburst that triggered the IXPE observation. A single power-law model with a free photon index is used to determine the photon fluxes. The two gray shaded regions demarcate two previous IXPE observations, while the red shaded area indicates the observation discussed in this paper.

Table 5
Multiwavelength Polarization Observations of BL Lacertae During the IXPE Pointing

Telescope	Π (%)	σ_{Π}	ψ (deg)	σ_{ψ}
KVN (22 GHz)	5.710 ± 0.066	...	16 ± 5	...
KVN (43 GHz)	6.020 ± 0.138	...	6 ± 1	...
KVN (86 GHz)	4.309 ± 0.621	...	172 ± 7	...
KVN (129 GHz)	6.978 ± 0.493	...	154 ± 4	...
POLAMI (3 mm)	7.27 ± 0.43	...	5.7 ± 1.5	...
POLAMI (1.3 mm)	8.08 ± 1.38	...	-6.5 ± 4.2	...
SMA (1.3 mm)	6.22 ± 0.88	...	1.9 ± 0.3	...
Calar Alto and SNO (<i>R</i> band)	10.9 ± 0.3	1.74	178 ± 0.6	4.41
Perkins (<i>B</i> band)	10.33 ± 0.22	3.61	172 ± 0.6	11.19
Perkins (<i>V</i> band)	9.66 ± 0.15	3.21	173 ± 0.4	11.44
Perkins (<i>R</i> band)	9.28 ± 0.2	4.10	175 ± 0.7	13.51
Perkins (<i>I</i> band)	10.23 ± 0.2	3.33	168 ± 1	8.08

Note. The uncertainties in Π and ψ are either the uncertainty of the measurement or, in the case of multiple measurements, the median uncertainty. σ_{Π} and σ_{ψ} show the standard deviation of the observations.

data reduction and polarization calibration was performed following Kang et al. (2015). We find similar results with $\Pi_R \sim 6\%$ and ψ_R between 16° and 154° . The IRAM-30 m observations were obtained and analyzed as part of the POLAMI⁷⁰ program (Agudo et al. 2018b, 2018a; Thum et al. 2018). The polarization degree of BL Lacertae was measured to be $\Pi_R = 8.08 \pm 1.38\%$ along position angle $\psi_R = -6.5^\circ \pm 4.2^\circ$ at 1.3 mm, and $\Pi_R = 7.27 \pm 0.43\%$, $\psi_R = 5.7^\circ \pm 1.5^\circ$ at 3.5 mm. No circular polarization was detected ($<1.1\%$, 99% confidence interval) at 1.3 mm and $<0.6\%$ (99% confidence interval) at 3.5 mm. The SMA (Ho et al. 2004) observation was taken within the framework of the SMA Monitoring of AGNs with Polarization (SMAPOL) program with the SMA polarimeter (Marrone & Rao 2008). The polarized quantities are derived from the Stokes I , Q , and U visibilities and calibrated with the mid-IR software package.⁷¹ The measurements yield $\Pi_R = 6.22 \pm 0.88\%$ along $\psi_R = 1.9^\circ \pm 0.3^\circ$, consistent with the contemporaneous POLAMI observation.

Optical polarization coverage was provided by the Calar Alto (Calar Alto Faint Object Spectrograph, CAFOS; *R* band), Higashi–Hiroshima Observatory (Kanata telescope) with the Hiroshima Optical and Near-InfraRed camera (HONIR; *R* and *J* band), NOT with the Alhambra Faint Object Spectrograph and Camera (ALFOSC; in *BVR*), the 1.8 m Perkins Telescope (*BVR*), and the Sierra Nevada Observatory (SNO; *R* band). A detailed description of the observing strategy and data reduction of the aforementioned telescopes can be found in Kawabata et al. (1999), Akitaya et al. (2014), Hovatta et al. (2016), Marscher & Jorstad (2021), Liidakis et al. (2022), and Middei et al. (2023), respectively, and references therein. The observations cover the entire duration of the IXPE observation, revealing high variability of the polarization degree, from $\sim 3\%$ to $\sim 17\%$, with EVPA fluctuating about the direction of the jet axis, $10^\circ \pm 2^\circ$ (Weaver et al. 2022). Figure 7 displays the optical observations, while Table 5 summarizes the radio and optical polarization results for the individual telescopes.

⁷⁰ <http://polami.iaa.es/>.









⁷¹ <https://lweb.cfa.harvard.edu/~cqi/mircook.html>.

The three day binned Fermi-LAT γ ray light curve of BL Lacertae is given in Figure 8, extracted from the Fermi-LAT Light Curve Repository (Soheila et al. 2023), with IXPE observation times highlighted. The third IXPE observation of BL Lacertae, reported here, occurred during an outburst.

ORCID iDs

Abel L. Peirson  <https://orcid.org/0000-0001-6292-1911>
 Michela Negro  <https://orcid.org/0000-0002-6548-5622>
 Ioannis Liidakis  <https://orcid.org/0000-0001-9200-4006>
 Riccardo Middei  <https://orcid.org/0000-0001-9815-9092>
 Dawoon E. Kim  <https://orcid.org/0000-0001-5717-3736>
 Alan P. Marscher  <https://orcid.org/0000-0001-7396-3332>
 Herman L. Marshall  <https://orcid.org/0000-0002-6492-1293>
 Luigi Pacciani  <https://orcid.org/0000-0001-6897-5996>
 Roger W. Romani  <https://orcid.org/0000-0001-6711-3286>
 Kinwah Wu  <https://orcid.org/0000-0002-7568-8765>
 Alessandro Di Marco  <https://orcid.org/0000-0003-0331-3259>
 Niccoló Di Lalla  <https://orcid.org/0000-0002-7574-1298>
 Nicola Omodei  <https://orcid.org/0000-0002-5448-7577>
 Svetlana G. Jorstad  <https://orcid.org/0000-0001-6158-1708>
 Iván Agudo  <https://orcid.org/0000-0002-3777-6182>
 Giacomo Bonnoli  <https://orcid.org/0000-0003-2464-9077>
 Beatriz Agís-González  <https://orcid.org/0000-0001-7702-8931>
 César Husillos  <https://orcid.org/0000-0001-8286-5443>
 Alessandro Marchini  <https://orcid.org/0000-0003-3779-6762>
 Alfredo Sota  <https://orcid.org/0000-0002-9404-6952>
 Carolina Casadio  <https://orcid.org/0000-0003-1117-2863>
 Juan Escudero  <https://orcid.org/0000-0002-4131-655X>
 Ioannis Myserlis  <https://orcid.org/0000-0003-3025-9497>
 Mark Gurwell  <https://orcid.org/0000-0003-0685-3621>
 Ryo Imazawa  <https://orcid.org/0000-0002-0643-7946>
 Yasushi Fukazawa  <https://orcid.org/0000-0002-0921-8837>
 Koji S. Kawabata  <https://orcid.org/0000-0001-6099-9539>
 Tsunefumi Mizuno  <https://orcid.org/0000-0001-7263-0296>
 Hiroshi Akitaya  <https://orcid.org/0000-0001-6156-238X>
 Nicoló Cibrario  <https://orcid.org/0000-0003-3842-4493>
 Immacolata Donnarumma  <https://orcid.org/0000-0002-4700-4549>
 Juri Poutanen  <https://orcid.org/0000-0002-0983-0049>
 Fabrizio Tavecchio  <https://orcid.org/0000-0003-0256-0995>
 Lucio A. Antonelli  <https://orcid.org/0000-0002-5037-9034>
 Matteo Bachetti  <https://orcid.org/0000-0002-4576-9337>
 Luca Baldini  <https://orcid.org/0000-0002-9785-7726>
 Wayne H. Baumgartner  <https://orcid.org/0000-0002-5106-0463>
 Ronaldo Bellazzini  <https://orcid.org/0000-0002-2469-7063>
 Stefano Bianchi  <https://orcid.org/0000-0002-4622-4240>
 Stephen D. Bongiorno  <https://orcid.org/0000-0002-0901-2097>
 Raffaella Bonino  <https://orcid.org/0000-0002-4264-1215>
 Alessandro Brez  <https://orcid.org/0000-0002-9460-1821>
 Niccoló Bucciantini  <https://orcid.org/0000-0002-8848-1392>
 Fiamma Capitanio  <https://orcid.org/0000-0002-6384-3027>
 Simone Castellano  <https://orcid.org/0000-0003-1111-4292>
 Elisabetta Cavazzuti  <https://orcid.org/0000-0001-7150-9638>
 Chien-Ting Chen  <https://orcid.org/0000-0002-4945-5079>

Stefano Ciprini  <https://orcid.org/0000-0002-0712-2479>
 Enrico Costa  <https://orcid.org/0000-0003-4925-8523>
 Alessandra De Rosa  <https://orcid.org/0000-0001-5668-6863>
 Ettore Del Monte  <https://orcid.org/0000-0002-3013-6334>
 Victor Doroshenko  <https://orcid.org/0000-0001-8162-1105>
 Michal Dovčiak  <https://orcid.org/0000-0003-0079-1239>
 Steven R. Ehlert  <https://orcid.org/0000-0003-4420-2838>
 Teruaki Enoto  <https://orcid.org/0000-0003-1244-3100>
 Yuri Evangelista  <https://orcid.org/0000-0001-6096-6710>
 Sergio Fabiani  <https://orcid.org/0000-0003-1533-0283>
 Riccardo Ferrazzoli  <https://orcid.org/0000-0003-1074-8605>
 Javier A. Garcia  <https://orcid.org/0000-0003-3828-2448>
 Shuichi Gunji  <https://orcid.org/0000-0002-5881-2445>
 Jeremy Heyl  <https://orcid.org/0000-0001-9739-367X>
 Wataru Iwakiri  <https://orcid.org/0000-0002-0207-9010>
 Philip Kaaret  <https://orcid.org/0000-0002-3638-0637>
 Vladimir Karas  <https://orcid.org/0000-0002-5760-0459>
 Jeffery J. Kolodziejczak  <https://orcid.org/0000-0002-0110-6136>
 Henric Krawczynski  <https://orcid.org/0000-0002-1084-6507>
 Fabio La Monaca  <https://orcid.org/0000-0001-8916-4156>
 Luca Latronico  <https://orcid.org/0000-0002-0984-1856>
 Simone Maldera  <https://orcid.org/0000-0002-0698-4421>
 Alberto Manfreda  <https://orcid.org/0000-0002-0998-4953>
 Frédéric Marin  <https://orcid.org/0000-0003-4952-0835>
 Andrea Marinucci  <https://orcid.org/0000-0002-2055-4946>
 Francesco Massaro  <https://orcid.org/0000-0002-1704-9850>
 Giorgio Matt  <https://orcid.org/0000-0002-2152-0916>
 Fabio Muleri  <https://orcid.org/0000-0003-3331-3794>
 C.-Y. Ng  <https://orcid.org/0000-0002-5847-2612>
 Stephen L. O'Dell  <https://orcid.org/0000-0002-1868-8056>
 Chiara Oppedisano  <https://orcid.org/0000-0001-6194-4601>
 Alessandro Papitto  <https://orcid.org/0000-0001-6289-7413>
 George G. Pavlov  <https://orcid.org/0000-0002-7481-5259>
 Melissa Pesce-Rollins  <https://orcid.org/0000-0003-1790-8018>
 Pierre-Olivier Petrucci  <https://orcid.org/0000-0001-6061-3480>
 Maura Pilia  <https://orcid.org/0000-0001-7397-8091>
 Andrea Possenti  <https://orcid.org/0000-0001-5902-3731>
 Simonetta Puccetti  <https://orcid.org/0000-0000-0000-0000>
 Brian D. Ramsey  <https://orcid.org/0000-0003-1548-1524>
 John Rankin  <https://orcid.org/0000-0002-9774-0560>
 Ajay Ratheesh  <https://orcid.org/0000-0003-0411-4243>
 Oliver J. Roberts  <https://orcid.org/0000-0002-7150-9061>
 Carmelo Sgró  <https://orcid.org/0000-0001-5676-6214>
 Patrick Slane  <https://orcid.org/0000-0002-6986-6756>
 Gloria Spandre  <https://orcid.org/0000-0003-0802-3453>
 Douglas A. Swartz  <https://orcid.org/0000-0002-2954-4461>
 Toru Tamagawa  <https://orcid.org/0000-0002-8801-6263>
 Roberto Taverna  <https://orcid.org/0000-0002-1768-618X>
 Allyn F. Tennant  <https://orcid.org/0000-0002-9443-6774>
 Nicholas E. Thomas  <https://orcid.org/0000-0003-0411-4606>

Francesco Tombesi  <https://orcid.org/0000-0002-6562-8654>
 Alessio Trois  <https://orcid.org/0000-0002-3180-6002>
 Sergey Tsygankov  <https://orcid.org/0000-0002-9679-0793>
 Roberto Turolla  <https://orcid.org/0000-0003-3977-8760>
 Jacco Vink  <https://orcid.org/0000-0002-4708-4219>
 Martin C. Weisskopf  <https://orcid.org/0000-0002-5270-4240>
 Fei Xie  <https://orcid.org/0000-0002-0105-5826>
 Silvia Zane  <https://orcid.org/0000-0001-5326-880X>

References

- Abdo, A. A., Ackermann, M., Ajello, M., et al. 2010, *ApJ*, 710, 1271
 Agudo, I., Thum, C., Molina, S. N., et al. 2018a, *MNRAS*, 474, 1427
 Agudo, I., Thum, C., Ramakrishnan, V., et al. 2018b, *MNRAS*, 473, 1850
 Ajello, M., Angioni, R., Axelsson, M., et al. 2020, *ApJ*, 892, 105
 Akitaya, H., Moritani, Y., Ui, T., et al. 2014, *Proc. SPIE*, 9147, 914740
 Albert, J., Aliu, E., Anderhub, H., et al. 2007, *ApJ*, 666, L17
 Arlen, T., Aune, T., Beilicke, M., et al. 2013, *ApJ*, 762, 92
 Baldini, L., Bucciantini, N., Lalla, N. D., et al. 2022, *SoftX*, 19, 101194
 Blandford, R., Meier, D., & Readhead, A. 2019, *ARA&A*, 57, 467
 Blinov, D., Pavlidou, V., Papadakis, I., et al. 2015, *MNRAS*, 453, 1669
 Blinov, D., Pavlidou, V., Papadakis, I., et al. 2018, *MNRAS*, 474, 1296
 Casadio, C., MacDonald, N. R., Boccardi, B., et al. 2021, *A&A*, 649, A153
 Cerruti, M., Zech, A., Boisson, C., et al. 2019, *MNRAS*, 483, L12
 Chen, L. 2014, *ApJ*, 788, 179
 Di Marco, A., Soffitta, P., Costa, E., et al. 2023, *AJ*, 165, 143
 Gao, S., Fedynitch, A., Winter, W., & Pohl, M. 2019, *NatAs*, 3, 88
 Giommi, P., Perri, M., Capalbi, M., et al. 2021, *MNRAS*, 507, 5690
 Ho, P. T. P., Moran, J. M., & Lo, K. Y. 2004, *ApJ*, 616, L1
 Hovatta, T., Lindfors, E., Blinov, D., et al. 2016, *A&A*, 596, A78
 Hughes, P. A., Aller, H. D., & Aller, M. F. 1985, *ApJ*, 298, 301
 Icecube Collaboration, Aartsen, M., Ackermann, M., et al. 2018, *Sci*, 361, 147
 Kang, S., Lee, S.-S., & Byun, D.-Y. 2015, *JKAS*, 48, 257
 Kawabata, K. S., Okazaki, A., Akitaya, H., et al. 1999, *PASP*, 111, 898
 Kiehlmann, S., Blinov, D., Liodakis, I., et al. 2021, *MNRAS*, 507, 225
 Kintscher, T., Icecube Collaboration, Fact Collaboration, et al. 2017, in International Cosmic Ray Conference, 35, 969
 Kraus, A., Krichbaum, T. P., Wegner, R., et al. 2003, *A&A*, 401, 161
 Krawczynski, H. 2012, *ApJ*, 744, 30
 Liodakis, I., Marscher, A. P., Agudo, I., et al. 2022, *Natur*, 611, 677
 Marrone, D. P., & Rao, R. 2008, *Proc. SPIE*, 7020, 70202B
 Marscher, A. P. 2014, *ApJ*, 780, 87
 Marscher, A. P., & Jorstad, S. G. 2021, *Galax*, 9, 27
 Marscher, A. P., Jorstad, S. G., D'Arcangelo, F. D., et al. 2008, *Natur*, 452, 966
 Marscher, A. P., Jorstad, S. G., Larionov, V. M., et al. 2010, *ApJ*, 710, L126
 Middei, R., Giommi, P., Perri, M., et al. 2022, *MNRAS*, 514, 3179
 Middei, R., Liodakis, I., Perri, M., et al. 2023, *ApJL*, 942, L10
 Myserlis, I., Angelakis, E., Kraus, A., et al. 2018, *A&A*, 609, A68
 Peirson, A. L., Liodakis, I., & Romani, R. W. 2022, *ApJ*, 931, 59
 Peirson, A. L., & Romani, R. W. 2018, *ApJ*, 864, 140
 Peirson, A. L., & Romani, R. W. 2019, *ApJ*, 885, 76
 Raiteri, C. M., Villata, M., D'Ammando, F., et al. 2013, *MNRAS*, 436, 1530
 Sahakyan, N., & Giommi, P. 2022, *MNRAS*, 513, 4645
 Soheila, A., Marco, A., Luca, B., et al. 2023, *ApJS*, 265, 31
 Tavecchio, F., Landoni, M., Sironi, L., & Coppi, P. 2018, *MNRAS*, 480, 2872
 Thum, C., Agudo, I., Molina, S. N., et al. 2018, *MNRAS*, 473, 2506
 Vermeulen, R. C., Ogle, P. M., Tran, H. D., et al. 1995, *ApJ*, 452, L5
 Vlahakis, N., & Königl, A. 2004, *ApJ*, 605, 656
 Weaver, Z. R., Jorstad, S. G., Marscher, A. P., et al. 2022, *ApJS*, 260, 12
 Weaver, Z. R., Williamson, K. E., Jorstad, S. G., et al. 2020, *ApJ*, 900, 137
 Wehrle, A. E., Grupe, D., Jorstad, S. G., et al. 2016, *ApJ*, 816, 53
 Weisskopf, M. C., Soffitta, P., Baldini, L., et al. 2022, *JATIS*, 8, 026002
 Xie, F., Ferrazzoli, R., Soffitta, P., et al. 2021, *APh*, 128, 102566
 Zhang, H., & Böttcher, M. 2013, *ApJ*, 774, 18